

# The Influence of Quark Matter at High Densities on Binary Neutron Star Mergers

R. Oechslin<sup>1\*</sup>, K. Uryū<sup>2</sup>, G. Poghosyan<sup>1</sup>, F. K. Thielemann<sup>1</sup>

<sup>1</sup>*Departement für Physik und Astronomie der Universität Basel, Klingelbergstr. 82, CH-4056 Basel, Switzerland*

<sup>2</sup>*SISSA, Via Beirut 2/4, 34014 Trieste, Italy*

20 March 2022

## ABSTRACT

We consider the influence of potential quark matter existing at high densities in neutron star interiors on gravitational waves (GW) emitted in a binary neutron star merger event. Two types of equations of state (EoS) at zero temperatures are used, one describing pure nuclear matter, the other nuclear matter with a phase transition to quark matter at very high densities. Binary equilibrium sequences close to the innermost stable circular orbit (ISCO) are calculated to determine the GW frequencies just before merger. It is found that EoS effects begin to play a role for gravitational masses larger than  $M_\infty \simeq 1.5M_\odot$ . The difference in the gravitational wave frequency at the ISCO grows to up to  $\simeq 10\%$  for the maximal allowed mass given by the EoSs used. Then, we perform 3D hydrodynamic simulations for each EoS varying the initial mass and determine the characteristic GW frequencies of the merger remnants. The implications of quark matter show up mainly in a different collapse behaviour of the merger remnant. If the collapse does not take place immediately after merger, we find a phase difference between two EoS's in the post-merger GW signal. We also compare the GW frequencies emitted by the merger remnant to values from simulations using a polytropic EoS and find an imprint of the non-constant adiabatic index of our EoSs. All calculations are based on the conformally flat (CF) approximation to general relativity and the GW signal from the merger simulation is extracted up to quadrupole order.

**Key words:** hydrodynamics, gravitational waves, equation of state, stars: neutron

## 1 INTRODUCTION

Binary neutron star mergers belong to the strongest gravitational wave sources for interferometer-type gravitational wave observatories as LIGO (Abramovici et al. 1992), VIRGO (Bradaschia et al. 1990), GEO600 (Lück 1997) and TAMA (Ando et al. 2001). After a long inspiral process which lasts millions of years, the final merger phase takes place on a millisecond timescale. The onset of merger is given when the two companions become dynamically unstable near the innermost stable circular orbit (ISCO) and mass transfer starts. Since the process has no definite symmetries, 3D hydrodynamic simulations are necessary. In addition, because of the compactness of the system, general relativistic effects have to be considered and treated as accurately as possible.

It has been pointed out that the gravitational wave frequency  $f_{GW}$  relates to the compactness  $(M/R)_\infty$  of a neu-

tron star as  $f_{GW} \sim (M/R)_\infty^{3/2}$  near the ISCO, meaning that the gravitational wave frequency just before merger carries information on the radius of the neutron star. Hence the GW signal may constrain the equation of state (EoS) of high density matter, (see e.g. Lai & Wiseman 1996; Rasio & Shapiro 1999). It has also been found recently that a neutron star formed after the merger may be supported by rapid and differential rotation even if its mass exceeds 60% of the maximum mass of a single non-rotating neutron star, and the GW are emitted due to non-axisymmetric and quasiradial oscillations of the remnant for longer than the dynamical timescale (Shibata & Uryū 2000, 2002; Shibata, Taniguchi & Uryū 2003). If these oscillations persist for a longer time, the integrated gravitational wave may be detectable, carrying information on the high density matter.

In addition to general relativistic gravity, various physics should be taken into account for many aspects of the binary neutron star merger problem such as the nuclear forces summarized in the EoS, neutrino physics and magnetic fields. So far, however, due to this complexity, investi-

\* present address: Max-Planck Institut für Astrophysik, Karl Schwarzschild-Str. 1, 85741 Garching, Germany

gations have concentrated either on the relativistic aspects of the problem using a simple EoS, or on the microphysical aspects while treating gravity in a Newtonian framework. The pioneering work was done by Oohara & Nakamura in (Oohara & Nakamura 1999, and references therein). Relativistic aspects have been considered using the post-Newtonian approximation (Ayal et al. 2001; Faber & Rasio 2002, and references therein), the conformally flat approximation (Mathews & Wilson 2000; Oechslin et al. 2002; Faber, Grandclément & Rasio 2003, and references therein) and a fully general relativistic treatment (Shibata & Uryū 2000, 2002; Shibata, Taniguchi & Uryū 2003, and references therein). Microphysical improvements have been applied by Ruffert & Janka (2001, and references therein) and Rosswog & Davies (2002, and references therein) using different EoSs (Shen et al. 1998; Lattimer & Swesty 1991) and a leakage scheme to account for neutrino emission after the merger. For a review on the topic, see (Rasio & Shapiro 1999).

In this paper, we focus on two EoS for high density neutron star matter, one describing pure nuclear matter, the other nuclear matter with a transition to a quark phase at very high densities. A reason for investigating these EoSs is that the quark phase transition may be one of the most dramatic phenomena to change the compactness of neutron stars, and therefore its influence may be clearly observed in the GW spectrum of an inspiralling binary system. Following our previous work (Oechslin et al. 2002), we consider the merger problem in the conformally flat approximation.

The paper is organised as follows. In sect. 2, we summarize the formalism to solve the Einstein and the relativistic hydrodynamic equations, and describe the numerical implementation, the choice of EoS and the initial conditions. In sect. 3, we present the results of the paper and finally, we draw conclusions in sect. 4.

## 2 FUNDAMENTAL INGREDIENTS

In this section we describe the numerical methods and the physics on which our simulations are based. We consider a general relativistic fluid whose internal properties are described by a given EoS. Two sets of equations have to be solved simultaneously. On one hand side, we consider the relativistic hydrodynamic equations governing the fluid motion on the other side the Einstein equation of general relativity determining the spacetime metric and therefore the gravitational interaction. On top of it, an EoS which closes the system of hydrodynamic equations, has to given as an input.

### 2.1 Relativistic Hydrodynamics and Approximation for General Relativistic Gravity

In the 3+1 decomposition of spacetime, the metric  $ds^2 = g_{\mu\nu}dx^\mu dx^\nu$  can be written as

$$ds^2 = (-\alpha^2 + \beta_i\beta^i)dt^2 + 2\beta_i dx^i dt + \gamma_{ij}dx^i dx^j, \quad (1)$$

where  $\alpha$  is the lapse function,  $\beta^i$  is the shift vector, and  $\gamma_{ij}$  is the spatial metric. Spacetime quantities are decomposed with respect to the foliation using the hypersurface normal

defined as  $n_\mu = -\alpha\partial_\mu t$  with  $n^\mu n_\mu = -1$  and a projection tensor defined as  $\gamma_{\mu\nu} = g_{\mu\nu} + n_\mu n_\nu$ , whose spatial component agrees with the spatial metric.

The Einstein field equations can be written as a set of two evolution equations

$$\begin{aligned} \partial_t \gamma_{ij} &= -2\alpha K_{ij} + \nabla_i \beta_j + \nabla_j \beta_i, \\ \partial_t K_{ij} &= \alpha [R_{ij} - 2K_{il}K_j^l + KK_{ij} \\ &\quad - 8\pi S_{ij} + 4\pi\gamma_{ij}(S - \rho_E)] \\ &\quad - \nabla_i \nabla_j \alpha + \beta^l \nabla_l K_{ij} + K_{il} \nabla_j \beta^l + K_{jl} \nabla_i \beta^l, \end{aligned} \quad (2)$$

and two constraint equations

$$R + K^2 - K_{ij}K^{ij} = 16\pi\rho_E, \quad (4)$$

$$\nabla_j (K^{ij} - \gamma^{ij}K) = 8\pi j^i \quad (5)$$

for the dynamic variables  $\gamma_{ij}$  and  $K_{ij}$ , the extrinsic curvature of the hypersurface (see e.g. Baumgarte and Shapiro 2003). Here,  $R_{ij}$  is the Ricci tensor and  $\nabla$  the covariant derivative associated with  $\gamma_{ij}$ . The stress energy tensor  $T_{\mu\nu}$  is decomposed into  $\rho_E = n^\mu n^\nu T_{\mu\nu}$ , the matter energy density,  $j^i = \gamma_\mu^i n_\nu T^{\mu\nu}$ , the matter momentum density and  $S_{ij} = \gamma_{i\mu} \gamma_{j\nu} T^{\mu\nu}$ , the spatial projection of the stress energy tensor. Finally,  $R, S$  and  $K$  denote the traces of  $R_{ij}, S_{ij}$  and  $K_{ij}$ , respectively.

In the following discussion, we consider a perfect fluid with a matter stress energy tensor

$$T_{\mu\nu} = \rho h u_\mu u_\nu + p g_{\mu\nu} \quad (6)$$

Here,  $\rho$  refers to the rest mass density,  $h = 1 + p/\rho + \epsilon$  to the specific relativistic enthalpy,  $\epsilon$  to the specific internal energy,  $u_\mu$  to the four velocity and  $p$  to the fluid pressure. Then,

$$\rho_E = \rho h (\alpha u^0)^2 - p \quad (7)$$

$$j^i = \rho h \alpha u^0 u^\mu \gamma_\mu^i. \quad (8)$$

The Lorentz factor  $W = \alpha u^0$  can be calculated using the normalisation condition  $u_\mu u^\mu = -1$ .

$$\alpha u^0 = (1 + \gamma^{ij} u_i u_j)^{1/2}. \quad (9)$$

Isenberg proposed a waveless approximation to general relativity, in which he truncates some terms in Einstein's equation written in the ADM formalism to deduce an elliptic type formalism (Isenberg 1978). Later, the same set of equations have been rediscovered by Wilson and Mathews (Wilson, Mathews & Marronetti 1996) and widely used to solve single or binary neutron stars problems. (e.g. Oechslin et al. 2002) as well as binary black hole systems (Grandclément, Gourgoulhon & Bonazzola 2002). The Isenberg-Wilson-Mathews theory has its own Hamiltonian as pointed out by Isenberg himself (also discussed in Friedman, Uryū & Shibata 2002).

In this approximation, the conformally flat condition for the spatial geometry  $\gamma_{ij} = \psi^4 \delta_{ij}$  and  $K = \partial_t K = 0$  are imposed, where  $\delta_{ij}$  is the flat 3-metric. It may be viewed that the second one is a choice of a temporal gauge condition, the maximal slicing condition, while the first one is an approximation as well as partly a spatial gauge choice (details can be found in Baumgarte et al. 1998). The remaining metric variables ( $\psi, \alpha, \beta^i$ ) do not satisfy all components of the Einstein's field equation consistently. We pick the constraints and the trace of the evolution equation for  $K_{ij}$  as

equations for the above five variables, which leads to the same set of equations derived from Isenberg's Hamiltonian mentioned above.

The approximation leads to a considerable simplification of the Einstein equations, since all metric equations can be written in elliptic form.

The trace of the evolution equation for  $K_{ij}$  together with the maximal slicing condition  $K = 0$  leads to an equation for the lapse

$$\Delta(\alpha\psi) = 2\pi\alpha\psi^5(\rho_E + 2S) + \frac{7}{8}\alpha\psi^5 K_{ij}K^{ij}, \quad (10)$$

The trace-free part of the evolution equation for  $\gamma_{ij}$  together with the conformally flat condition  $\gamma_{ij} = \psi^4\delta_{ij}$  provides

$$2\alpha\psi^{-4}K_{ij} = \partial_j\tilde{\beta}_i + \partial_i\tilde{\beta}_j - \frac{2}{3}\delta_{ij}\partial_k\beta^k, \quad (11)$$

where  $\partial_i$  is a derivative with respect to the coordinate associated with  $\delta_{ij}$  and  $\tilde{\beta}_i$  relate to the shift  $\beta^i$  through the flat metric as  $\tilde{\beta}_i = \delta_{ij}\beta^j$ . The Hamiltonian constraint provides an equation for the conformal factor

$$\Delta\psi = -2\pi\psi^5\rho_E - \frac{1}{8}\psi^5 K_{ij}K^{ij} \equiv 4\pi S_\psi. \quad (12)$$

Finally, with the momentum constraint we obtain an equation for the shift vector

$$\begin{aligned} \Delta\beta^i + \frac{1}{3}\partial^i\partial_j\beta^j &= \partial_j\ln\left(\frac{\alpha}{\psi^6}\right)\left(\partial^j\beta^i + \partial^i\beta^j - \frac{2}{3}\delta^{ij}\partial_l\beta^l\right) \\ &+ 16\pi\alpha\psi^4 j^i, \end{aligned} \quad (13)$$

where  $\partial^i = \delta^{ij}\partial_j$ . Using the definition

$$\beta^i = B^i - \frac{1}{4}\partial^i\chi, \quad (14)$$

(13) splits into two simpler parts

$$\Delta B^i = \partial_j\ln\left(\frac{\alpha}{\psi^6}\right)\left(\partial^j\beta^i + \partial^i\beta^j - \frac{2}{3}\delta^{ij}\partial_l\beta^l\right) + 16\pi\alpha\psi^4 j^i, \quad (15)$$

and

$$\Delta\chi = \partial_j B^j. \quad (16)$$

While the trace-free components of the evolution-equation for  $\gamma_{ij}$  (2) are used to relate  $K_{ij}$  and the metric variables as in equation (11), its trace part and the trace-free components of the evolution-equation for  $K_{ij}$  (3) are dropped by the CF approximation. The trace of (2) can be used to check the accuracy and reliability of the CF approximation (Dimmelmeier et al. 2002; Oechslin 2003)

The relativistic hydrodynamic equations can be written in the following way

$$\partial_t\rho^* + \partial_i(\rho^*v^i) = 0, \quad (17)$$

$$\begin{aligned} \partial_t(\rho^*\epsilon) + \partial_i(\rho^*\epsilon v^i) &= -p\left[\partial_t(\alpha u^0\gamma^{1/2})\right. \\ &\left.+ \partial_i(\alpha u^0\gamma^{1/2}v^i)\right], \end{aligned} \quad (18)$$

$$\partial_t(\rho^*hu_k) + \partial_i(\rho^*hu_kv^i) = -\alpha\gamma^{1/2}\partial_k p + \quad (19)$$

$$\rho^*h\left[-\alpha u^0\partial_k\alpha + u_j\partial_k\beta^j - \frac{u_i u_j}{2u^0}\partial_k\gamma^{ij}\right], \quad (20)$$

where

$$\rho^* = \rho\alpha u^0\det(\gamma_{ij}) \quad \text{and} \quad (21)$$

$$v^i = -\beta^i + \frac{\gamma^{ij}u_j}{u^0} \quad (22)$$

In the case of conformal flatness, the system reduces to

$$\frac{d}{dt}\rho^* = -\rho^*\partial_iv^i \quad (23)$$

$$\begin{aligned} \frac{d}{dt}\tilde{u}_i &= -\frac{1}{\rho^*}\alpha\psi^6\partial_ip - \alpha\tilde{u}^0\partial_i\alpha + \tilde{u}_j\partial_i\beta^j \\ &+ \frac{2\tilde{u}_k\tilde{u}_k}{\psi^5\tilde{u}^0}\partial_i\psi \end{aligned} \quad (24)$$

$$\frac{d}{dt}\epsilon = -\frac{p}{\rho^*}\partial_iv^i - \frac{p}{\rho^*}\partial_t\ln(\alpha u^0\psi^6), \quad (25)$$

with

$$\tilde{u}_i = hu_i, \quad (26)$$

$$\rho^* = \rho\alpha u^0\psi^6 \quad \text{and} \quad (27)$$

$$v^i = -\beta^i + \frac{\delta^{ij}u_j}{\psi^4 u^0} \quad (28)$$

Here, we have cast the system into a Lagrangian formulation which is better suited for an implementation on a computer using a Lagrangian scheme like SPH (cf. sect. 2.2). The conserved hydrodynamic variables are  $(\rho^*, \tilde{u}_i, \epsilon)$  whereas the primitive variables are  $(\rho, v^i, \epsilon)$ .

## 2.2 Numerical implementation

To solve the system of hydrodynamic equations (23) - (25) we use the Smoothed Particle Hydrodynamics method (SPH; (Benz 1990; Monaghan & Gingold 1983)), which is widely used in astronomical and astrophysical simulations. The original form of SPH that solves the Newtonian hydrodynamic equations is presented in (Benz 1990). We list here the generalized version which is appropriate for the above relativistic hydrodynamic equations. For details, see (Oechslin et al. 2002). The continuity equation turns into a relation between  $\rho^*$  and the rest masses of the individual particles

$$\rho_a^* = \sum_b m_b W_{ab}, \quad (29)$$

where  $m_b$  is the rest mass of particle  $b$  and  $W_{ab} = W(|\mathbf{r}_a - \mathbf{r}_b|, h_{SPH})$  denotes the weight given by the standard spherical spline Kernel function  $W(\mathbf{r}, h_{SPH})$ . The rest masses  $m_b$  and the smoothing length  $h_{SPH}$  are initially chosen to fit an initial spatial distribution of  $\rho^*$ . The pressure gradient contained in the momentum equation (25) is calculated as in standard SPH but replacing  $\rho$  by  $\rho^*$ ,

$$\frac{1}{\rho_a^*}\partial_ip_a = -\sum_b m_b\left(\frac{p_b}{\rho_b^{*2}} + \frac{p_a}{\rho_a^{*2}}\right)\partial_i W_{ab}. \quad (30)$$

The energy equation (25) contains a pdV-term similar to Newtonian SPH

$$-\frac{p}{\rho}\partial_iv^i\Big|_a = \frac{1}{2}\sum_b m_b\left(\frac{p_a}{\rho_a^*\rho_a} + \frac{p_b}{\rho_b^*\rho_b}\right)(v_a^i - v_b^i)\partial_i W_{ab}. \quad (31)$$

The additional terms in the momentum and energy equation that arise from the gravitational interaction are evaluated by

first solving the equations for the metric variables  $\alpha, \psi$  and  $\beta^i$  on a overlaid grid (see discussion below) and by mapping back those quantities onto the particles by second-order interpolation. The total time derivative of  $\ln(\alpha u^0 \psi^6)_a$  in the energy equation is evaluated using second order finite differencing in time.

On top of these equations, an artificial viscosity (AV) scheme is implemented with time-dependent viscosity parameters (Morris & Monaghan 1997) which have only significant values in the presence of shocks. The AV produces an additional viscous pressure which is added to the physical fluid pressure (Siegle & Riffert 2000).

The field equations (10,12,15 and 16) are discretized on a grid which covers the matter distribution. The evaluation proceeds generally in three steps

- First, we calculate the source corresponding to the potential. The involved hydrodynamic quantities defined on the SPH particles are transferred onto the grid by assigning SPH-interpolated values to the grid points, i.e.

$$\langle f(x) \rangle_{SPH} = \sum_j f_j \frac{m_j}{\rho_j^*} W(|\mathbf{r} - \mathbf{r}_j|, h_j). \quad (32)$$

- Afterwards, the potential is obtained by solving the corresponding Poisson-equation. The  $\psi$ - and the  $\alpha\psi$ -equation are closely linked together and are therefore solved in two iteration steps using the solution from the previous timestep as a guess. The remaining four equations determining the shift vector are also closely coupled and are solved simultaneously within the FMG algorithm.

- All needed derivatives are calculated on the grid using finite differencing.

- Finally, the potential and its derivatives are mapped back onto the SPH particle distribution using a triangular shaped cloud (TSC) method (Hockey & Eastwood 1992) known from particle mesh codes. This is equivalent to a second order interpolation.

Boundary conditions and extensions of the solution beyond the grid are obtained using a multipole expansion of the source term. For details we refer to (Oechslin et al. 2002).

Like the Newtonian and the first-order post-Newtonian (1PN) approximation, the CF approximation does not include gravitational radiation and its reaction by construction. We therefore have to add an additional gravitational wave (GW) extraction scheme and a radiation reaction force which accounts for the angular momentum and energy carried away by GW. The waveform in transverse-traceless gauge is extracted in the slow-motion limit (Thorne 1980; Wilson, Mathews & Marronetti 1996) and up to quadrupole order using

$$h_{ij}^{TT}(t, \mathbf{r}) = \frac{2}{r} P_{ijkl} \ddot{Q}_{kl}(t - r), \quad (33)$$

where

$$Q_{ij} = \text{STF} \left\{ -2 \int S_\psi(x) x_i x_j d^3x \right\} \quad (34)$$

is the mass-quadrupole of the system. The radiation-reaction force is chosen in a similar way to the original Burke-Thorne expression  $F_i^{rr} = \sigma \partial_i V$  with  $V = -1/5 x_i x_j Q_{ij}^{(5)}$ , but its strength  $\sigma$  is chosen such that the resulting angular momentum loss by backreaction  $\dot{J}_i^{tot} - \dot{J}_i^{num}$  reproduces the

expression

$$\dot{J}_i = -\frac{2}{5} \epsilon_{ijk} Q_{jm}^{(2)} Q_{km}^{(3)} \quad (35)$$

of the slow motion GW extraction approximation up to a difference of the order of  $\simeq 5\%$ . Since  $J_i = \epsilon_{ijk} \int \rho^* (x^j \tilde{u}_k - x^k \tilde{u}_j) d^3x$ , we can obtain the angular momentum change using

$$\dot{J}_i = \epsilon_{ijk} \int \rho^* \left( (x^j \dot{\tilde{u}}_k - x^k \dot{\tilde{u}}_j) + (v^j \tilde{u}_k - v^k \tilde{u}_j) \right) d^3x. \quad (36)$$

The expressions  $\dot{J}_i^{num}$ , the numerical angular momentum error, and  $\dot{J}_i^{tot}$ , the total angular momentum change per unit time, are obtained by evaluating (36) before adding and after adding the backreaction force terms, respectively. Since  $\dot{J}_i^{num}$  has an oscillating behaviour around zero, as a result thereof,  $\dot{J}_i^{tot}$  depends on the binary orbit. Therefore, in practical determination of the value of  $\sigma$ , we take an average  $\langle \dot{J}_i^{tot} - \dot{J}_i^{num} \rangle$  for about a half orbit, and compare with  $\langle \dot{J} \rangle$  computed from the quadrupole formula (35) that is averaged for the same orbit. For model B1 we obtain for the ratio  $\langle \dot{J}_i^{num} \rangle / \langle \dot{J}_i^{tot} \rangle \sim 0.3\%$  at the ISCO, where the average is made over one orbital period, while at a certain period of time  $\dot{J}_i^{num}$  may become comparable to  $\dot{J}_i^{tot}$ . Since the ratio  $\langle \dot{J}_i^{num} \rangle / \langle \dot{J}_i^{tot} \rangle$  is negligible, the radiation reaction force is clearly driving the inspiral process, although the predicted time to merger have to be taken with care due to the approximative radiation reaction scheme and the spatially conformal flat assumption used in our initial conditions and simulations. Fully relativistic inspiral simulations Miller, Gressman & Suen (2003) are intrinsically consistent concerning radiation reaction dissipation but they still depend on the outer boundary location.

### 2.3 Equation of state

To investigate the influence of quark matter to a neutron star merger, we consider two equations of state, an EoS describing pure nuclear matter (“hadronic EoS”) and an EoS describing nuclear matter with a phase transition to quark matter at very high densities (“hybrid EoS”).

The hadronic EoS is realized using the non-linear  $\sigma$ - $\omega$  model in the relativistic mean field approximation with the TM1 parameter set which is motivated by a least-square fit to experimental results including stable and unstable nuclei (Sugahara & Toki 1994). At densities above  $\rho \gtrsim 10^{14} \text{g/cm}^3$  this is a good approximation. For lower values, when inhomogeneous nuclear matter appears and the non-linear  $\sigma$ - $\omega$  model is not valid any more, other approximations have to be used (e.g. Shen et al. 1998). In our case, we append a polytropic EoS  $p = \kappa \rho^\Gamma$  where  $\kappa$  and  $\Gamma$  are adjusted to fulfill smoothness of pressure and internal energy. We choose the transition density to the polytropic EoS at  $2 \times 10^{14} \text{g/cm}^3$  which leads to  $\Gamma \simeq 2.86$ , similar to common realistic EoSs in this density regime. The hybrid EoS is obtained by combining the hadronic EoS with a MIT bag model (Chodos et al. 1974) using a variable pressure phase transition construction (Glendenning 1992). We use massless up and down quarks and a Bag constant of  $90 \text{MeV/fm}^3$ . The resulting hybrid EoS then describes three physical phases

- A pure hadronic phase below  $\approx 5 \times 10^{14} \text{g/cm}^3 \approx 1.8 \rho_0$

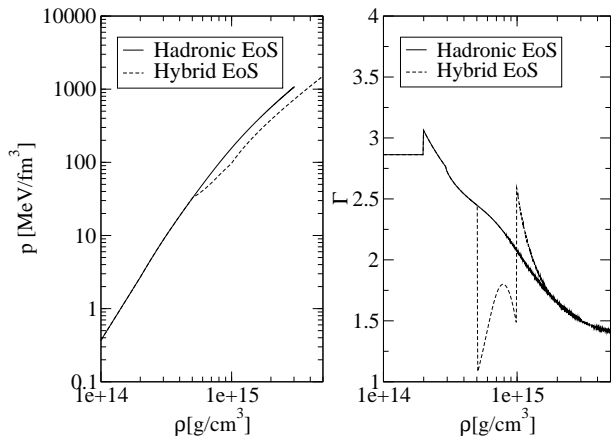


**Figure 1.** Comparison of the considered nuclear EoS. The hybrid EoS (dashed curve) has a phase transition region ( $1.8\rho_0 < \rho < 3.5\rho_0$ ) where adiabatic indices are substantially lower, followed by a quark phase which has a similar stiffness as the nuclear matter at those densities.

where the EoS coincides with the hadronic EoS. Here,  $\rho_0 := 2.8 \times 10^{14} \text{g/cm}^3$  is the nuclear saturation density. The stiffness in this region varies between  $\Gamma \approx 3$  and  $\Gamma \approx 2.5$ .

- A quark-hadron mixed phase between  $\approx 5 \times 10^{14} \text{g/cm}^3$  and  $\approx 10^{15} \text{g/cm}^3 \approx 3.5\rho_0$  where both quark and hadrons are present. In this phase transition region, the EoS substantially softens with  $\Gamma \approx 1 - 1.5$ .

- A pure quark phase above  $\approx 10^{15} \text{g/cm}^3$  where the MIT-bag-model EoS with similar adiabatic index but lower absolute pressure in comparison to the hadronic EoS is applied.

In both EoSs, we neglect temperature effects, i.e. we set  $T=0$ . The redundant internal energy information from the EoS is dropped and we consider the pressure as a function of the density alone. This is a good approximation in the high-density regime where thermal effects to the pressure are rather small. At lower densities (e.g. in the disk around the merger remnant) the thermal component is certainly not negligible. However we concentrate in this work on the high-density merger remnant so we claim to be rather accurate with this approximation although thermal effects could have an effect via neutrino losses.

## 2.4 Initial Conditions

To construct initial conditions, we assume the binary to be in a quasi-equilibrium state. This assumption is not very well satisfied in the very vicinity of the ISCO (Miller 2003) and we therefore choose slightly wider initial orbits. In our models the binaries have initially no radial velocity either and need about half an orbit to begin with the inspiral. We apply the method of Uryū & Eriguchi (2000) to construct an initial configuration. This method takes an EoS as an input and then solves the hydrostatic equation for an irrotational velocity field together with the Einstein field equations in the CF approximation. A similar method has been developed by (Bonazzola, Gourgoulhon & Marck 1999). We map

**Table 1.** Input parameters of the considered models using the hadronic and hybrid EoS.  $M_\infty$  denotes the gravitational mass of one NS in isolation and  $C$  is the compactness. Both the masses and the compactness refer to one binary component in isolation.  $N_{Particle}$  denotes the number of SPH particles and  $N_{Grid}$  is the number of grid points. In model E1,  $97^3$  gridpoints are used, but at the onset of collapse, the resolution is enhanced to  $129^3$ . Models with a '1' in the label are calculated with the hadronic EoS, models with a '2' used the hybrid EoS.

Model	$M_\infty [M_\odot]$	$C = (M/R)_\infty$	$N_{particle}$	$N_{Grid}$
A1	1.2	0.1276	154038	$97^3$
B1,B2	1.35	0.1424	153993	$97^3$
C1,C2	1.4	0.1475	169798	$97^3$
D1	1.5	0.1577	100488	$97^3$
D2	1.5	0.1579	100548	$97^3$
E1	1.75	0.1853	162536	$97^3(129^3)$
E2	1.75	0.1959	157222	$129^3$

**Table 2.** Selected properties of our initial models resulting from the input parameters shown in Table 1.  $M_0$  is the restmass of one single NS,  $P$  the orbital period,  $f_{GW,0}$  the corresponding GW frequency,  $d_0$  the initial orbital separation and  $R_\infty$  the radius of one single isolated NS measured in Schwarzschild coordinates. Note that the GW frequencies are lower than those in Fig. 2 which are taken at the ISCO.

Model	$M_0 [M_\odot]$	$P [ms]$	$f_{GW,0} = 2/P$	$d_0 [km]$	$R_\infty [km]$
A1	1.295	2.92	685	38.00	13.88
B1,B2	1.471	2.72	737	36.93	13.99
C1,C2	1.523	2.65	756	36.71	14.01
D1	1.649	2.57	777	36.19	14.03
D2	1.649	2.57	777	36.19	14.02
E1	1.957	2.20	909	33.40	13.93
E2	1.959	1.97	1058	31.14	13.07

the output of the above method, the hydrodynamic quantities and the conformal factor onto a distribution of SPH particles. Finally, this SPH distribution is relaxed to avoid spurious inter-particle forces using a braking term

$$\mathbf{f} = -\frac{1}{\tau_{relax}}(\mathbf{v} - \mathbf{v}_{irr}), \quad (37)$$

where  $\mathbf{v}_{irr}$  is the given initial irrotational velocity field of the initial mass distribution. Using this method, we produce a set of irrotational quasi-equilibrium configurations, both varying the EoS and the gravitational mass  $M_\infty$ , where  $M_\infty$  refers to the mass of a single NS in isolation. For  $M_\infty$ , we use values between  $M_\infty = 1.2M_\odot$  which is at the lower limit of the observational range and  $M_\infty = 1.75M_\odot$  which is close to the maximal gravitational NS mass of  $M_{max} = 1.78M_\odot$  of the hybrid EoS. The models are summarized in Tab. 1. The letter part (A-E) in the model label indicates the mass while the number part (1,2) indicates the EoS. All orbits are taken slightly outside the ISCO, about  $12 \sim 25\%$  in coordinate separation. This results in smaller lag angles and its oscillations in the initial phase since tidal forces are weaker at larger separation. In Tab. 2, we summarize properties which result as a consequence of the chosen initial parameters in Tab. 1.

### 3 RESULTS

In this section, we consider the final evolution of the binary NS from a circular orbit configuration to one single object, a transient NS or a BH. This evolution takes place on a dynamical timescale and is triggered by radiation reaction. While in Sec. 3.1, the EoS effects on the GW frequency from the final inspiral phase just before a merger has been discussed, in the latter subsections the result of the dynamical evolution of the binary NS from stable circular orbit to the merger is presented.

#### 3.1 EoS impact on the quasi-equilibrium binary

By considering the compactness  $(M/R)_\infty$  in Tab.1, we observe that the properties of the models become EoS dependent for the most massive cases D1, D2 and E1, E2, i.e. when  $M_\infty \gtrsim 1.5M_\odot$ . For lower stellar masses, the NSs do not reach the phase transition density  $\rho_t := 1.8\rho_0$  in the center and an EoS effect cannot be observed. It has been shown that the orbital frequency and the gravitational wave frequency of a binary system depends on the compactness of its components (e.g. Lai & Wiseman 1996; Uryū et al. 2000; Faber et al. 2003). Therefore we expect that an EoS effect may be seen in the GW frequency at the final stage of inspiral in our models.

Using the method of (Uryū & Eriguchi 2000; Uryū et al. 2000), we systematically investigated the locations of the ISCO, beyond which the binary become dynamically unstable, and the GW frequency at the ISCO. As shown in Fig. 2(a), an EoS effect becomes important above  $M_\infty = 1.5M_\odot$ . The reason is that at this mass, the central density reaches the phase transition density to mixed matter in the hybrid case and a dense core of mixed matter is formed. For even larger masses, the transition density to pure quark matter at  $\rho \simeq 3.5\rho_0$  is reached and a quark core is formed. Due to this, a neutron star with the hybrid EoS becomes more compact than one with the hadronic EoS as shown in Fig. 2(b), which is reflected in the difference in the GW frequency. Near the maximal NS mass of the hybrid EoS, the GW frequency of the hybrid EoS binary is up to 10% larger than that of the hadronic EoS binary. Such a change of tendency for increasing gravitational wave frequency with respect to increasing mass at  $M_\infty \gtrsim 1.5M_\odot$  may suggest an existence of a drastic change of EoS such as a quark phase transition.

#### 3.2 Dynamical Evolution of the Neutron Star Merger

We now turn to the merger phase that follows the quasi-stationary inspiral when the two NS cross the ISCO and become dynamically unstable. To first illustrate the overall dynamics, we plot in Fig. 3 the density distribution for model B1 together with the velocity field in the corotating frame, whose angular velocity is determined as

$$\Omega = \frac{\sum_i m_i \omega_i}{\sum_i m_i} \quad (38)$$

where  $i$  runs over all particles and  $\omega_i$  denotes the angular velocity of the individual particles. The stars are counterrotating relative to the corotating frame and tidal lag

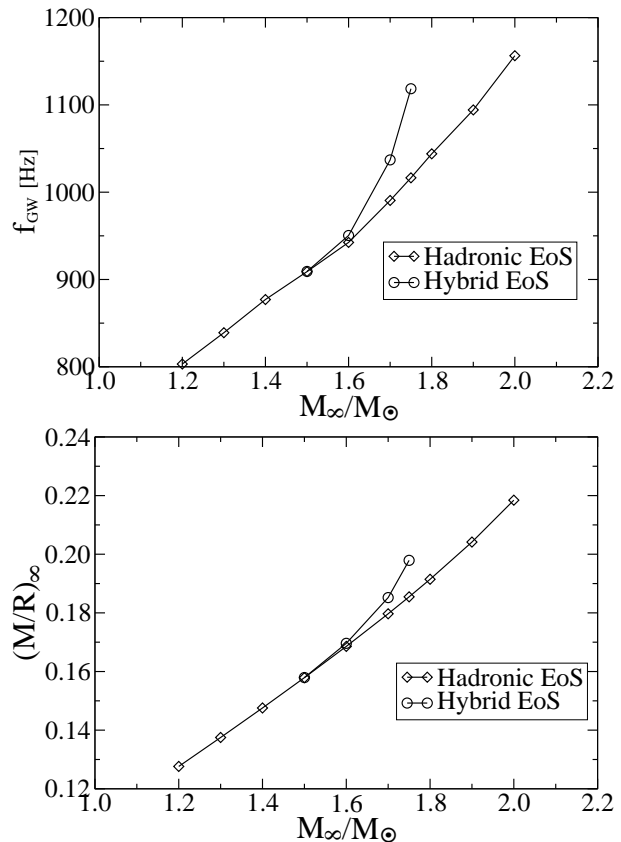


**Figure 2.** (a)GW frequencies depending on the gravitational mass in isolation at the ISCO. (b)Compactness of an isolated neutron star with respect to the gravitational mass.

angles are developing (snapshot 1). At merger, this counterrotation is first turned into a shear motion at the contact layer and then into a pattern of vortex rolls due to the growing Kelvin-Helmholtz instability (snapshot 2,3). Finally we end up with a differentially rotating, non-axisymmetric merger remnant (snapshot 4). In Fig. 4, we concentrate on the evolution of the merger remnant during the first milliseconds by plotting the density contour linearly which allows a better visualisation of the high-density central parts (The lowest density contour is at  $5 \times 10^{13} \text{g/cm}^3$ .) In this figure we can see that during a phase of  $\sim 2\text{ms}$  after merger, the core actually consists of two small subcores which are leftovers of the original NS cores. Visible is also that the two subcores still carry a small counterrotating motion - a direct consequence of the irrotating setup - which disappears continuously until we end up in an nearly axisymmetric, differentially rotating configuration. It is reported from finite difference simulations (e.g. Shibata & Uryū 2002; Shibata, Taniguchi & Uryū 2003) that this twin-core pattern persists for a longer time than our simulations. This may be a consequence of the numerical viscosity in our code.

#### 3.3 EoS differences in maximal density

To investigate the different consequences of the EoSs in detail, we first consider the evolution of the maximum density during the merger phase. We split the whole merger event in a pre-merger evolution where the binary still consists of

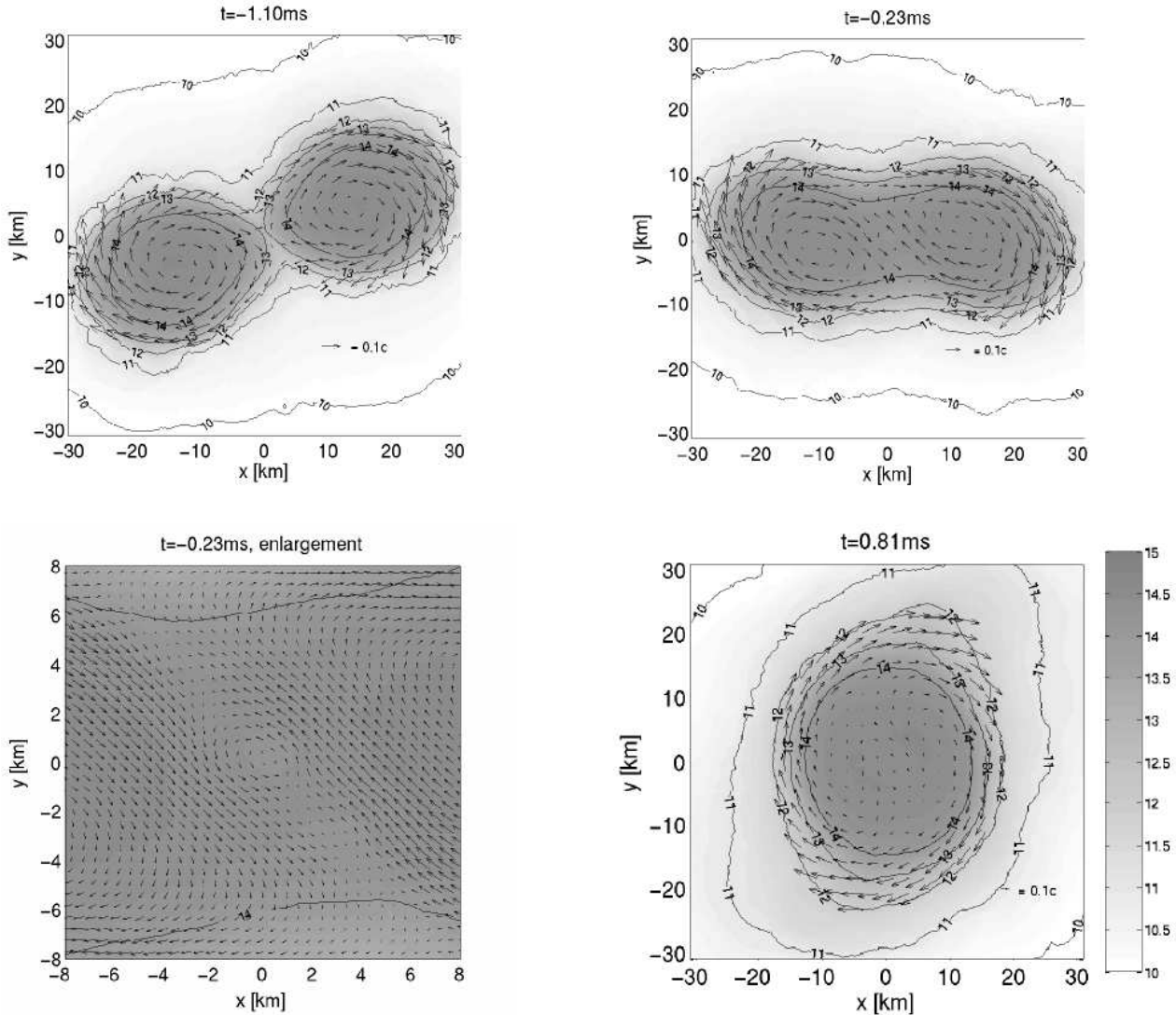


**Figure 3.** Snapshots at selected times of the baryonic density distribution and the velocity field of model B1 during pre-merger and merger evolution. The density is plotted logarithmically in units of  $\text{g}/\text{cm}^3$ , the velocity field is plotted in the corotating frame.

two tidally stretched objects and in a following post-merger evolution where a merger remnant, a NS or BH is forming. Since the SPH particle density  $\rho_a$  has no direct physical meaning, the actual density  $\rho(x)$  has to be calculated as a statistical average over the particles densities  $\rho_a$ . To find the maximal density, we first determine density values on selected gridpoints and then look for their maximum. Both the statistical averaging and the finite grid spacing introduce a small noise. In general, the evolution of  $\rho_{max}$ , plotted in Fig. 5 for our simulations, shows a slow decrease during the pre-merger phase when the two stars become tidally stretched and reaches its minimum during the actual merger. This is the case when the GW luminosity either approaches its max-

imum and the two NS are maximally tidally stretched or just a bit later when a new merger remnant has already formed but a twin-core structure is still present (see sect. 3.2). After the minimum, we can distinguish three possible evolutionary scenarios of  $\rho_{max}$ , depending on the collapse behaviour of the remnant. If the remnant can be stabilized by pressure and centrifugal forces,  $\rho_{max}$  slowly increases and then becomes constant. The second scenario is the delayed collapse where  $\rho_{max}$  first slowly increases on several dynamical timescales. This fragile equilibrium is concluded by a final collapse, which is visible as a steep rise of  $\rho_{max}$ . The last scenario is the immediate collapse just after the merger. Here,  $\rho_{max}$  increases without delay on a dynamical timescale.

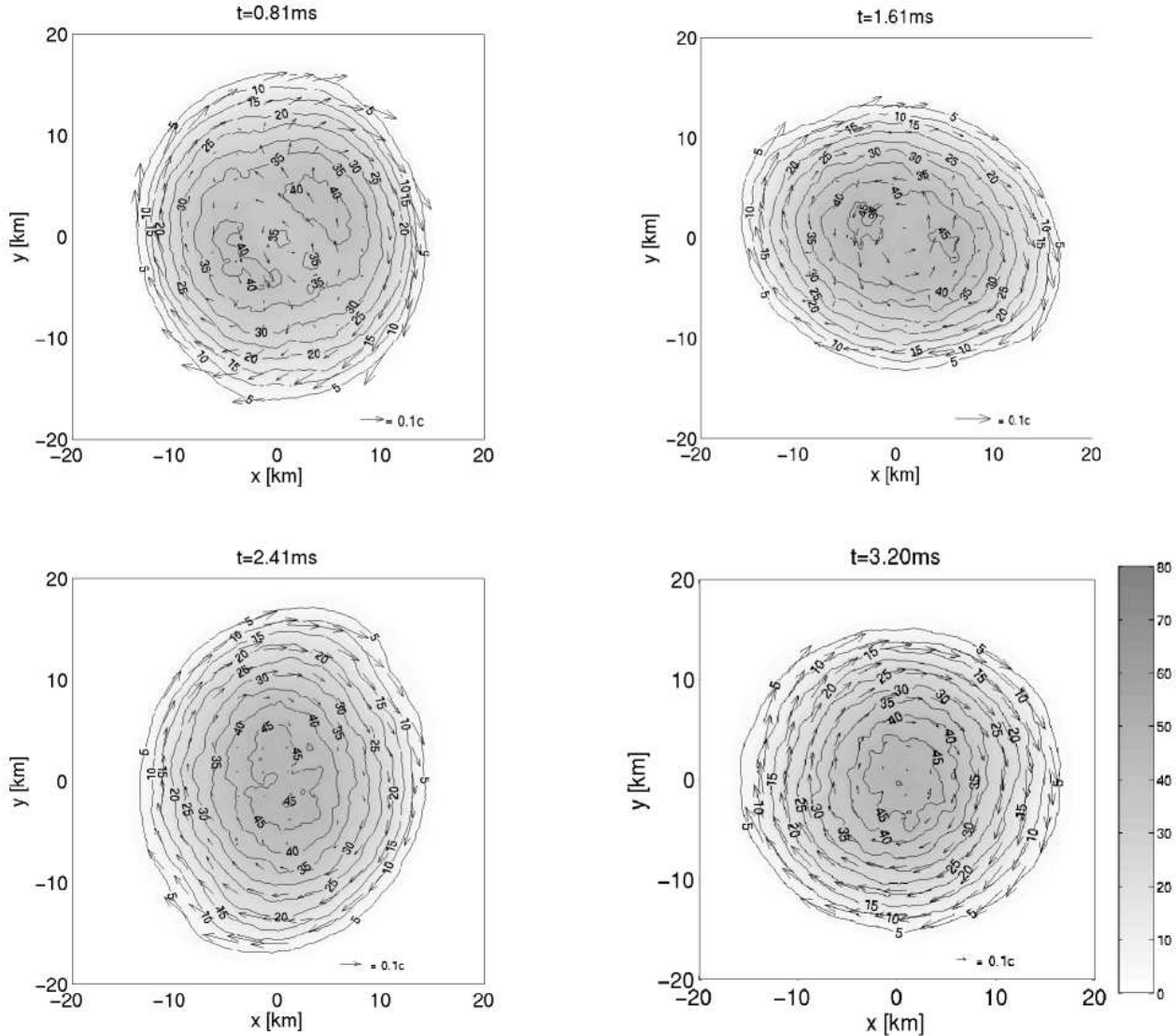


**Figure 4.** Same as Fig.3 but for the post-merger evolution. The density is plotted linearly in units of  $10^{13}\text{g}/\text{cm}^3$ .

Differences in the merger dynamics caused by the EoS, appear when  $\rho_{max}$  crosses the phase transition density  $\rho_t$ . At this point the hybrid EoS and therefore the dynamical evolution of the hybrid models separates from that of the hadronic EoS. If the individual stars are more massive than  $M_\infty \simeq 1.5M_\odot$ , their central density exceeds the phase transition density  $\rho_t$ . In this case, EoS differences happen already before merger. This makes a very small effect which even disappears close to merger due to tidal distortion if  $M_\infty$  is just at the threshold of  $\simeq 1.5M_\odot$  as in model D1/D2. On the other hand, if  $M_\infty$  is close to the maximal gravitational mass of the hybrid EoS as in model E1/E2, the EoS difference in  $\rho_{max}$  increases to up to  $\sim 60\%$ . Differences are also measurable for global quantities like the angular velocity of the binary, the compactness and especially for the GW frequency (cf. sect. 3.1). If the initial mass is less than  $M_\infty \simeq 1.5M_\odot$  an EoS difference can only be seen after the merger as part of a different evolution scenario of the merger remnant. Typically, the remnant collapses immediately or after a couple of dynamical timescales in the hybrid cases

while it settles down to a transient NS in the hadronic cases. Among the hadronic models, there is only the very massive model E1 which collapses immediately. In model D1, the maximal density slowly increases but does not really settle down - a sign that this object might eventually collapse. However, this might well be a numerical effect as angular momentum is transported from the core to the outer layers and differential rotation is slowly converted into uniform rotation. The amount which is transported is on the order of 40-50% in the very center during the whole evolution, despite of a very good overall angular momentum conservation, either by numerical viscosity or by gravitational interaction between the non-axisymmetric core and the outer layers. However it is still possible to stabilize a remnant with a gravitational mass of nearly  $3M_\odot$  with an EoS having a maximal gravitational mass of  $2.2M_\odot$  for about 12ms  $\simeq 820M_{tot}$ , where  $M_{tot} = 2.98M_\odot$  is the initial gravitational mass for this model. This stabilisation effect due to differential rotation has been pointed out in (Shibata & Uryū 2000; Baumgarte et al. 2000). The less massive models C1,B1 and



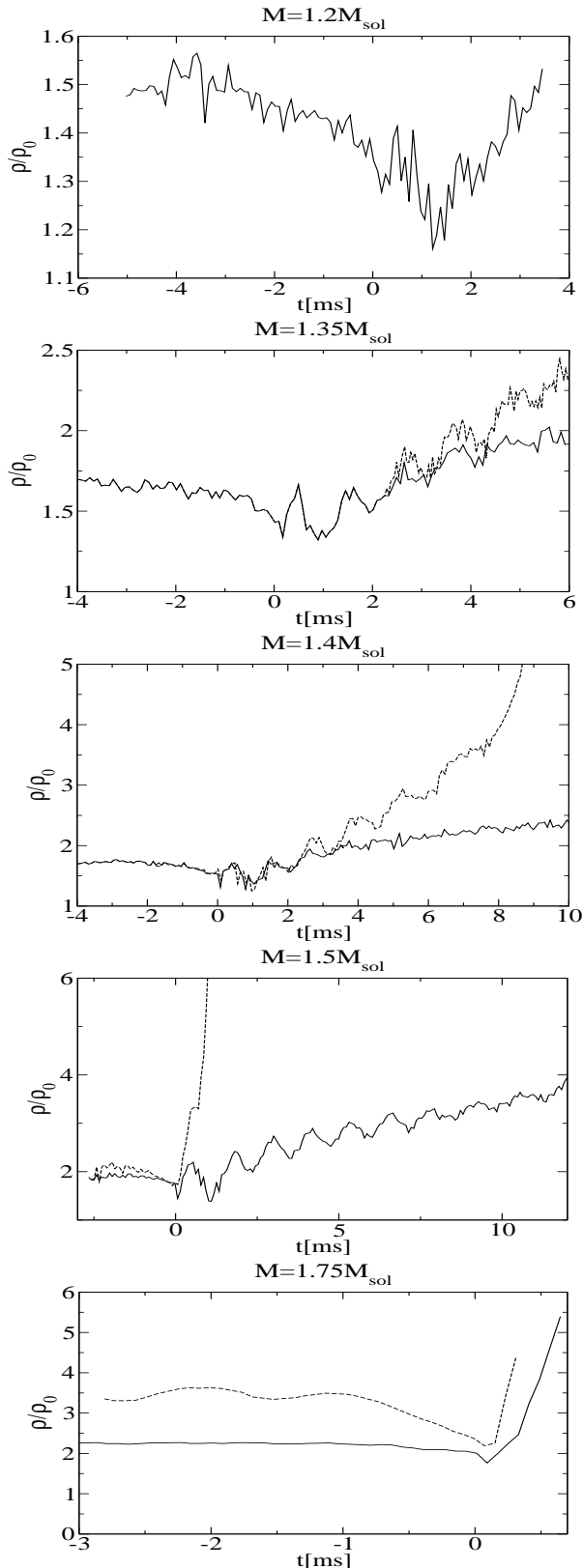


**Figure 5.** Evolution of the maximal density measured in units of the nuclear saturation density  $\rho_0 := 2.8 \times 10^{14} \text{g/cm}^3$ . The origin of the time axis has been shifted to the GW luminosity maximum. Solid lines correspond to hadronic models, dashed lines to hybrid models.

A1 lead to transient NS which do not collapse on a hydrodynamic timescale. On the hybrid-EoS model side, the models collapse with different collapse timescales. While models E2 and D2 collapse immediately, C2 collapses with a delay of about  $\sim 9$ ms. Model B2 does not collapse within the simulation time but it also shows a continuously growing maximum density. However, these collapse timescales are likely to be dominated by the above mentioned angular momentum transport.

### 3.4 The Gravitational Wave signal

A second indicator of EoS effects is the GW signal. Since the waveform is sensitive to dynamical mass motions we expect that all the above maximal density differences are reflected in the GW signal mainly in the form of different frequencies. In Fig. 6 we plot the waveforms of all models sorted according to the initial mass. Model E1/E2, the most massive one is the only one which shows a significant pre-merger EoS difference in the waveform. This is because the above mentioned maximal density difference translates via the compactness and the binary angular velocity into a GW frequency difference which amounts to  $\sim 10\%$  at the ISCO (cf. Fig. 2) while it disappears during the actual merger phase. The next less massive model, D1/D2, does not show any EoS differences in the GW frequency at the ISCO and further during the pre-merger phase, but we may expect, that for larger binary distances and therefore smaller tidal interaction, GW frequency differences could be seen. The more interesting part of this model is the different collapse behaviour and therefore the totally different waveform. While the hybrid model D2 only produces a short, high-frequent burst before the collapse, the hadronic model emits a long wavetrain which decreases slowly in amplitude. Models C1/C2 and B1/B2 emit both a quasi-periodic (QP) GW-signal which is characteristic for the rotation and oscillation mode in the merger remnant. EoS-differences in the waveform do not appear until a considerable mixed matter core has formed in the hybrid case. As a consequence, the first part of the post-merger GW signal, which is the strongest in our simulations, will not be affected by any EoS difference. However, when the mixed matter core becomes large enough, an accumulating phase shift in the waveform becomes clearly visible. In the C1/C2-model the shift adds up to more than half a period before the collapse of the hybrid remnant happens, in the B1/B2 model, the shift is only very small, but visible.

### 3.5 Gravitational Wave Spectra

The Fourier spectrum of the GW waveform is plotted in Fig.7. The most massive E1/E2-model shows its EoS differences in the pre-merger part, i.e in the frequency domain around 1kHz. Here the spectrum produced by the pre-merger hybrid waveform is significantly stronger than the one of the hadronic waveform, since the amplitude of wave strain  $h$  scales roughly as  $(r/M)h \sim (M/R)_\infty$  where  $r$  is a distance from a source. This is consistent with simulations using quasi-equilibrium sequences (Faber et al. 2003). There is no contribution on the high frequency side from this model since both remnants collapse immediately after merger. Note that we miss the waveform emitted by the ringing of the resulting BH. However, the expected frequency of this signal

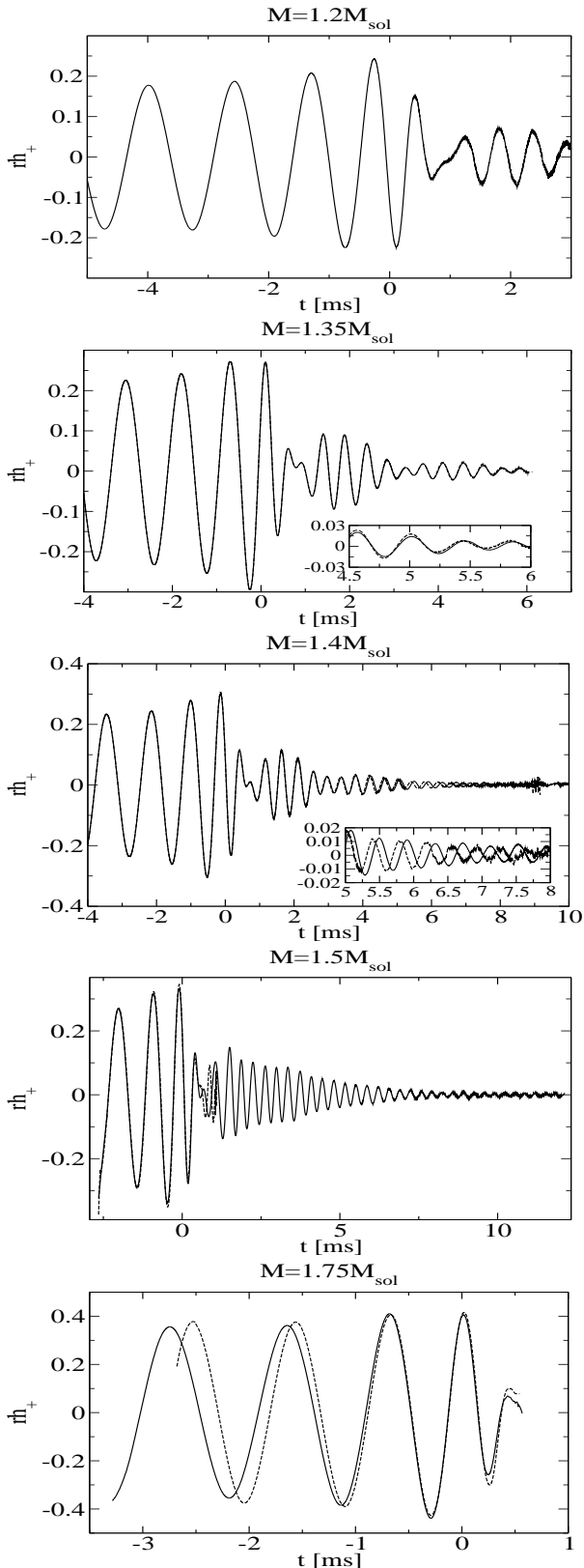


**Figure 6.** Gravitational waveforms of all models sorted according to their initial mass. The origin of the time axis has been shifted to the GW luminosity maximum. Solid lines correspond to hadronic models, dashed lines to hybrid models.

lies in the range of 5 – 10kHz (Shibata & Uryū 2002; Leaver 1985) we can clearly separate out the BH waveform.

The other models show their EoS-differences via different frequency peaks which result from the QP-waveform emitted in the post-merger. The difference is most obvious in the D1/D2-model. For the hadronic EoS model D1, a distinct Fourier peak is clearly visible, whereas the hybrid EoS model D2 leads only to a much weaker and very broad Fourier peak since the remnant is collapsing very soon after merging producing a much shorter post-merger GW signal. In the C1/C2-model, both the hadronic and the hybrid models have strong QP peaks where the one of the C2-model is slightly shifted to higher frequencies due to the more compact remnant. The same can be seen for the model B1/B2. However, effects here are smaller and a measurement may be difficult. The EoS-effects are this tiny because the spectrum is dominated by the first GW burst after merging which is insensible to EoS-differences.

We may compare the obtained QP frequencies  $f_{QP}$  to values from a fully relativistic calculation (Shibata & Uryū 2002) where an irrotational initial velocity field with a polytropic EoS is considered. Two peaks are found in their spectrum

$$f_{QP1} \sim 1.8f_{QE} \quad (39)$$

$$f_{QP2} \sim 2.8f_{QE} \quad (40)$$

for an adiabatic index of  $\Gamma = 2.25$  and

$$f_{QP1} \sim 1.8f_{QE} \quad (41)$$

$$f_{QP2} \sim 3.0f_{QE} \quad (42)$$

for  $\Gamma = 2$ . Here,  $f_{QE}$  is the GW frequency of the binary at the ISCO. (Shibata & Uryū 2002) point out, that  $f_{QP2}/f_{QE}$  is not very dependent on the initial compactness of the stars but the higher peak  $f_{QP2}/f_{QE}$  depends on  $\Gamma$  in a way that softer EoSs lead to higher values for  $f_{QP2}/f_{QE}$ . Since we use realistic EoSs with a non-constant  $\Gamma$  in our simulations, we expect the ratio  $f_{QP2}/f_{QE}$  to vary with increasing compactness (Zang, Centrella & McMillan 1996; Faber & Rasio 2001; Oechslin et al. 2002). Indeed our values for  $f_{QP2}/f_{QE}$  are strongly dependent on the initial mass  $M_\infty$  and compactness as can be seen in Tab. 3. From the behaviour of  $f_{QP2}/f_{QE}$  we can deduce that the EoS softens for more compact models, i.e. the EoS softens at higher densities. It might be very interesting to calculate the  $f_{QP2}/f_{QE}-(M/R)_\infty$ -relation for various other realistic EoSs on the market. Measuring this relation might give a detailed insight to the NS EoS in the nuclear regime above  $10^{14} \text{g/cm}^3$ .

One might expect that  $f_{QP2}$  is overestimated in our simulations due the already mentioned numerical viscosity effects in the code which leads to a slowly contracting merger remnant and therefore to emission of GW with higher frequencies. To check that this is not the case, we have also calculated the spectra of the truncated wavesignals which only contain the first few oscillations of the post-merger signals. The resulting QP peaks are reduced in strength but their positions remains unchanged within the uncertainty of the peak width (see Fig. 7).

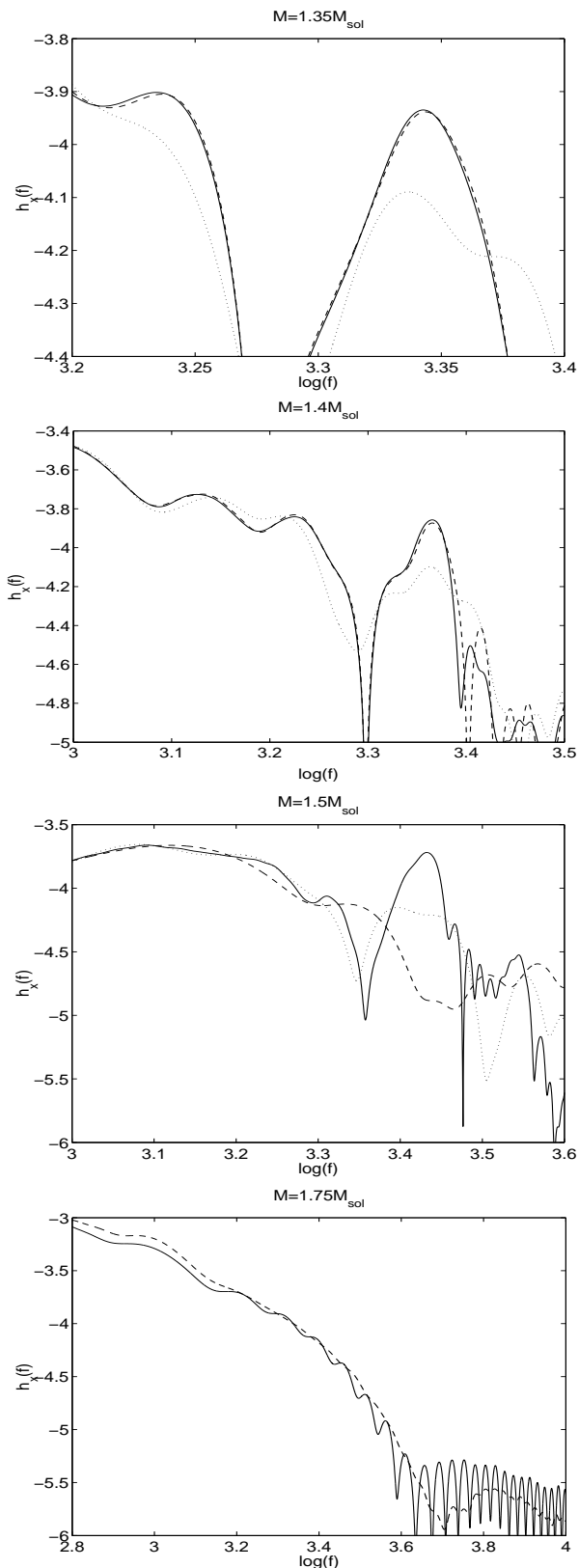


**Figure 7.** Fourier spectrum of the waveform  $h_+$  for models B1/B2 to E1/E2 sorted according to their initial mass. The frequency is in units of kHz. Solid lines correspond to hadronic models, dotted lines to the spectra of the corresponding truncated waveforms (see text) and the dashed lines correspond to hybrid models.

**Table 3.** Ratio of  $f_{QP2}$  to  $f_{QE}$  for all models where a transient NS forms or a delayed collapse happens. The values for  $f_{QE}$  are determined from quasi-equilibrium models and are taken at the ISCO.

Model	$M_\infty[M_\odot]$	$C = (M/R)_\infty$	$f_{QP2}[\text{kHz}]$	$f_{QP2}/f_{QE}$
A1	1.2	0.128	1.98	2.47
B1/B2	1.35	0.143	2.20	2.56
C1/C2	1.4	0.148	2.32	2.65
D1	1.5	0.158	2.70	2.97

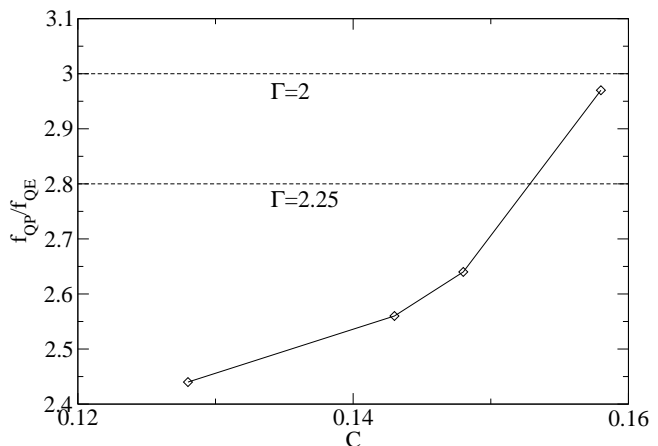


**Figure 8.** Relation between the ratio  $f_{QP2}/f_{QE}$  and the compactness  $C = (M/R)_\infty$ . The diamonds correspond to the hadronic EoS-models A1 to D1, the values for  $\Gamma = 2$  and  $\Gamma = 2.25$  are taken from (Shibata & Uryū 2002)

## 4 CONCLUSIONS

In this work, we have considered the impact of the EoS to the inspiral and merger dynamics of a binary neutron star coalescence. We have performed equilibrium sequence studies to investigate the GW frequencies around the ISCO. Then, dynamical simulations of the merging event using a 3-dimensional SPH code have been carried out. We have chosen a hadronic EoS based on the relativistic mean field approximation and a hybrid EoS which is obtained by combining the hadronic EoS with a MIT-bag-model-EoS in the high-density regime above  $\rho_t = 1.8\rho_0$ . The gravitational wave frequency at the ISCO depends strongly on the initial mass of the binary. For a generic mass of  $2 \times 1.4M_\odot$ , we find a GW frequency of around 900Hz for both EoSs. EoS differences become important for models with initial gravitational masses larger than  $M_\infty \sim 1.5M_\odot$ . At this mass range, the central density of the individual stars reach the phase transition  $\rho_t$  included in the hybrid EoS model. At masses close to the maximum gravitational mass of the hybrid EoS,  $M = 1.78M_\odot$ , the relative difference in  $f_{GW}$  becomes as large as  $\sim 10\%$ .

The maximum density evolution during the merger depends sensitively on the fact whether the phase transition density is crossed and at which time. For very massive models like models E1/E2 with an initial mass of  $M_\infty = 1.75M_\odot$  this is already fulfilled by the individual companion stars in the pre-merger phase. Less massive models with masses below  $M_\infty \lesssim 1.5M_\odot$  cross this threshold later in the post-

merger phase when the matter is contracting to form a transient NS or a BH. The hadronic EoS models all form a transient NS except the very massive E1 model which collapses immediately. In the D1 model, the maximum density does not converge after 12ms but rises slowly and continuously. We think that this is an effect of a considerable angular momentum transport from the remnant core to the outer layers which implies a continuous conversion of the differential rotation pattern into uniform rotation. All hybrid EoS models collapse on timescales which is highly dependent on the model mass. While the massive models E2 and D2 collapse immediately, models C2 and B2 collapse after a contraction of the remnant on several dynamical timescales and a considerable decrease of the degree of differential rotation. This indicates that the collapse is driven in this case by angular momentum transport caused e.g. by numerical viscosity. The collapse dynamics of these models will be investigated in future work. The emitted gravitational waveforms are very dependent on the initial mass of the model. The most massive model E1/E2 shows a large difference prior to merger both in frequency and amplitude. This is a consequence of the different compactnesses for the models E1 and E2 due to the different EoSs. The same effect is not visible in the less massive models because the compactness difference due to the EoSs vanishes. A second aspect of the GW signal is the waveform emitted by the remnant. If the remnant does not collapse immediately to a BH, a quasi-periodic waveform with a frequency of 2-3kHz is emitted. The ratio of this frequency to the GW frequency at the ISCO  $f_{QP2}/f_{QE}$  depends sensitively on the model and therefore on the mass or compactness  $(M/R)_\infty$ . Since  $f_{QP2}/f_{QE}$  is fairly constant for an EoS with constant stiffness, we interpret this result as a consequence of the varying stiffness of our EoS used. Hence, the relation  $f_{QP2}/f_{QE}-(M/R)_\infty$  is characteristic for the behaviour of the EoS's stiffness. A measurement of this quantity would provide important additional information of the EoS.

It has been suggested in Hughes (2002) that measurements of high frequency GW will require a network of broadband detectors combined with narrowband detectors that have a good sensitivity in the high frequency domain. Such measurements of high frequency GW may become feasible in the future and discover or constrain the existence of phase transition in neutron star matter at high densities.

### Acknowledgments

Computations were done at the Department for Physics and Astronomy at the University of Basel. RO would like to thank T. Janka for discussions and helpful comments. KU would like to thank M. Shibata and J. L. Friedman for discussion.

RO, GP and FKT are funded by the Schweizerischer Nationalfonds under grant 2000-061822.00.

### REFERENCES

Abramovici A. et al., 1992, *Science*, 256, 325; A. Abramovici et al., 1996, *Phys. Lett. A*, 218, 157

Ando M. et al., the TAMA collaboration, 2001, *Phys. Rev. Lett.*, 86, 3950.  
 Arnowitt R., Deser S., Misner C. W., in Witten, L., *Gravitation: An introduction to current research*, Wiley, NY, p. 226  
 Ayal S., Piran T., Oechslin R., Davies M., Rosswog R., 2001, *ApJ*, 550, 846  
 Baumgarte T. W., Shapiro S. L., 2003, *Phys. Rept.* 376, 41  
 Baumgarte T. W., Cook G. B., Scheel M. A., Shapiro S. L., Teukolsky S. A., 1998, *Phys. Rev. D*, 57, 7299  
 Baumgarte T. W., Shapiro S. L., Shibata M., 2000, *Astrophys. J.*, 528, L29  
 Baumgarte T. W., Shapiro S. L., *Phys. Rep.*, 2003, 376, 41  
 Benz W., 1990, in Buchler, J. R., ed., *The Numerical Modeling of Nonlinear Stellar Pulsations: Problems and Prospects*, Kluwer, Dordrecht, p. 269  
 Bonazzola S., Gourgoulhon E., Marck J.-A., 1999, *Phys. Rev. Lett.*, 82, 892  
 Bradaschia C. et al., 1990, *Nucl. Instrum. Methods A*, 289, 518  
 Chodos A. et al., 1974, *Nucl. Phys Rev. D*, 9, 3471-3495  
 Dimmelmeier H., Font. J. A., Müller E., *Astron. Astrophys.*, 2002, 388, 917  
 Faber J. A., Rasio F. A., 2002, *Phys. Rev. D.*, 65, 084042  
 Faber J. A., Rasio F. A., 2001, *Phys. Rev. D.*, 63, 044012  
 Faber J. A., Grandclément P., Rasio F. A., gr-qc/0312097, submitted to *Phys. Rev. D*  
 Faber J. A., Grandclément P., Rasio F. A., Taniguchi K., astro-ph/0204397, accepted by *Phys. Rev. Lett.*  
 Friedman J.L, Uryū K, Shibata M, 2002, *Phys. Rev. D* 65, 064035  
 Glendenning N. K., 1992, *Phys. Rev. D*, 46, 1274  
 Grandclement P, Gourgoulhon E, Bonazzola S, 2002, *Phys. Rev. D* 65, 044021  
 Hockney R. W., Eastwood J. W., 1994, *Computer Simulation Using Particles*, Institute of Physics, London  
 Hughes S. A., 2002, *Phys. Rev. D* 66, 102001  
 Isenberg J., Nester J., in *General Relativity and Gravitation* Vol.1, edited by A. Held, (Plenum Press, New York 1980); "Waveless Approximation Theories of Gravity", report (1978), University of Maryland.  
 Lattimer J. M., Swesty F. D., 1991, *Nucl. Phys.*, A535, 331  
 Leaver E.W., 1985, *Proc. R. Soc. London A*, 402, 285  
 Lai D., Wiseman A. G., 1996, *Phys. Rev. D* 54, 3958  
 Lück H., 1997, *Class. Quant. Grav.*, 14, 1471  
 Mathews G. R., Wilson J. R., 2000, *Phys. Rev. D*, 61, 127304  
 Miller M, 2003, gr-qc/0305024  
 Miller M, Gressman P, Suen W - M, 2003, gr-qc/0312030  
 Monaghan J, Gingold R, 1983, *J. Comp. Phys.*, 52, 374  
 Morris, J., Monaghan, J., 1997, *J. Comp. Phys.*, 136, 41  
 Oechslin R., Rosswog S., Thielemann F. K., 2002, *Phys. Rev. D* 65, 103005  
 Oechslin R., PhD. Thesis, University of Basel, 2003, Basel  
 Oohara K., Nakamura, T., 1999, *Prog. Theor. Phys. Suppl.*, 136, 270  
 Rasio F. A. & Shapiro S. L., 1999, *Class. Quant. Grav.*, 16, R1-R29  
 Rosswog S, Davies M. B., 2002, *MNRAS*, 3, 481; Rosswog S, Liebendörfer M., 2003, astro-ph/0302301, submitted to *MNRAS*  
 Ruffert M., Janka H. T., *Astron. Astrophys.*, 380, 544

- Shapiro S. L., Teukolsky S. A., 1983, *Black Holes, White Dwarfs, and Neutron Stars*, Wiley, New York
- Shen H., Toki H., Oyamatsu K., Sumiyoshi K., 1998, *Prog. Theor. Phys.*, 100, 1013
- Shibata M, Uryū K, 2000, *Phys. Rev. D*, 61, 064001
- Shibata M, Uryū K, 2002, *Prog. Theor. Phys.* 107, 265
- Shibata M, Taniguchi K, Uryū K, 2003, *Phys. Rev. D*, in press
- Siegler S., Riffert H., 2000, *ApJ*, 531, 1053
- Sugahara, Y, Toki, H, 1994, *Nucl. Phys.* A579, 557
- Thorne K. S., 1980, *Rev. Mod. Phys.* 52, 299
- Uryū K., Eriguchi Y., 2000, *Phys. Rev. D*, 61, 124023
- Uryū K., Shibata M., Eriguchi Y, 2000, *Phys. Rev. D*, 62, 104015
- Wilson J. R., Mathews G. J., Marronetti P., 1996, *Phys. Rev. D*, 54, 1317
- Zang X., Centrella J.M., McMillan S.L.W., 1996, *Phys. Rev. D*, 50, 7261